Volume 8 | Number 33 | 7 September 2016 | Pages 15089–15360

Nanoscale

www.rsc.org/nanoscale

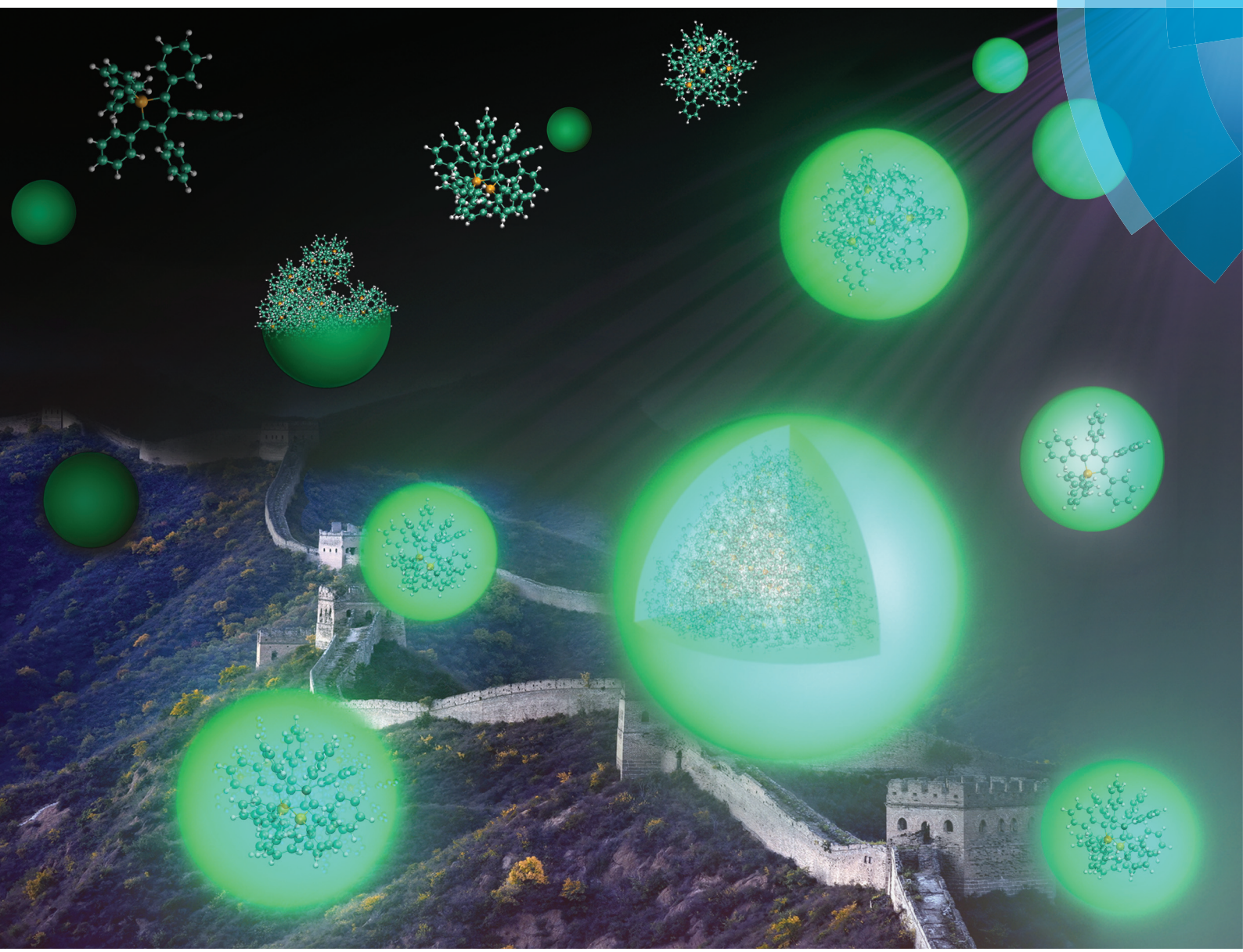

ISSN 2040-3364

ROYAL SOCIETY OF CHEMISTRY

PAPER

Qian Peng, Xuhui Huang, Zhigang Shuai *et al.*

Unraveling the aggregation effect on amorphous phase AIE luminogens: a computational study

NCNST

Nanoscale

PAPER

View Article Online
View Journal | View Issue

Cite this: *Nanoscale*, 2016, **8**, 15173

Unraveling the aggregation effect on amorphous phase AIE luminogens: a computational study†

Xiaoyan Zheng,[a] Qian Peng,*[b] Lizhe Zhu,[a] Yujun Xie,[c] Xuhui Huang*[a,e] and Zhigang Shuai*[d]

Received 3rd May 2016,
Accepted 17th June 2016

DOI: 10.1039/c6nr03599j

www.rsc.org/nanoscale

To achieve the efficient and precise regulation of aggregation-induced emission (AIE), unraveling the aggregation effects on amorphous AIE luminogens is of vital importance. Using a theoretical protocol combining molecular dynamics simulations and quantum mechanics/molecular mechanics calculations, we explored the relationship between molecular packing, optical spectra and fluorescence quantum efficiency of amorphous AIE luminogens hexaphenylsilole (HPS). We confirmed that the redshifted emission of amorphous aggregates as compared to crystalline HPS is caused by the lower packing density of amorphous HPS aggregates and the reduced restrictions on their intramolecular low-frequency vibrational motions. Strikingly, our calculations revealed the size independent fluorescence quantum efficiency of nanosized HPS aggregates and predicted the linear relationship between the fluorescence intensity and aggregate size. This is because the nanosized aggregates are dominated by embedded HPS molecules which exhibit similar fluorescence quantum efficiency at different aggregate sizes. In addition, our results provided a direct explanation for the crystallization-enhanced emission phenomenon of propeller-shaped AIE luminogens in experiments. Our theoretical protocol is general and applicable to other AIE luminogens, thus laying solid foundation for the rational design of advanced AIE materials.

Introduction

Fluorescent luminophores hold great potential in organic light emitting diodes, biological and environmental sensors, and bioimaging agents, due to their great variability and flexibility in materials synthesis.[1–5] Luminophores are typically utilized in the form of thin films and amorphous aggregates, however, practical applications of luminophores in solid states have long been prevented by aggregation-caused quenching (ACQ) effects.[6] This obstacle due to ACQ was not overcome until the discovery of exceptional luminophores that exhibit enhanced emission in the solid states.[7–9] The aggregation-induced emission (AIE) developed in 2001[10] offers a straightforward approach toward conquering ACQ and opens new avenues to achieve efficient light emission in the solid states.[11–17] However, how exactly the aggregation induces the emission of AIE luminogens remains controversial. Depending on the type and phases of AIE luminogens, their optical properties are usually dramatically different. For example, the AIE-active propeller-shaped siloles in the amorphous phase show redder and weaker fluorescence than their crystalline counterparts,[18] while the aggregation enhanced emission active amorphous-phased 2-amino-3-((*E*)-(4-(diethylamino)benzylidene)amino) maleonitrile (A3MN) exhibits considerably bluer and stronger fluorescence than that of the crystalline phase.[19]

Although decades of investigations have established the central role of the restriction of intramolecular motions (RIM) in the AIE mechanism,[2,20,21] the detailed structure–property relationship behind AIE remains elusive, largely due to the limited temporal and spatial resolution accessible to current experimental techniques. Theoretically, the AIE mechanism of AIE luminogens in gas and crystalline phases has been investigated through the hybrid quantum mechanics/molecular mechanics (QM/MM) calculations.[22] By contrast, few studies have been performed to elucidate the AIE mechanism in the amorphous phase – the form in which the majority of AIE products are obtained in experiments.

[a]*Department of Chemistry, The Hong Kong University of Science and Technology, Clear Water Bay, Kowloon, Hong Kong, China. E-mail: xuhuihuang@ust.hk*
[b]*Key Laboratory of Organic Solids, Beijing National Laboratory for Molecular Science (BNLMS), Institute of Chemistry, Chinese Academy of Sciences, Beijing 100190, P. R. China. E-mail: qpeng@iccas.ac.cn*
[c]*Department of Chemistry, Wuhan University, Wuhan 430072, P.R. China*
[d]*Key Laboratory of Organic OptoElectronics and Molecular Engineering, Department of Chemistry, Tsinghua University, Beijing 100084, P. R. China. E-mail: zgshuai@tsinghua.edu.cn*
[e]*Hong Kong Branch of Chinese National Engineering Research Center for Tissue Restoration & Reconstruction, Hong Kong University of Science and Technology, Clear Water Bay, Kowloon, Hong Kong, China*

†Electronic supplementary information (ESI) available: Supplementary methods, supplementary discussions, supplementary figures and tables. See DOI: 10.1039/c6nr03599j

A theoretical investigation of the aggregation effects on amorphous-phase AIE luminogens is a great challenge owing to the structural heterogeneity of the aggregates. Unlike their counterparts in the gas phase or in the crystalline phase, AIE luminogens in the amorphous state could not be represented by an aggregate of the solely fixed conformation but an ensemble of aggregates with numerous irregular conformations. Liang *et al.* have calculated the electronic spectra of the amorphous dimethoxy-tetraphenylethene aggregates formed in aqueous solution,[23] yet without reporting the excited-state nonradiative decay processes that have been considered decisive for the AIE effect.[24,25] Therefore, it is necessary to systematically unravel the aggregation effects on the photophysical properties of the amorphous AIE luminogens and to elucidate the exact roles of molecular packing in AIE materials.

Here we adopt a theoretical protocol combining molecular dynamics (MD) simulations and the correlation function rate formalism coupled QM/MM calculations to systematically explore the excited-state decay rates and vibrationally resolved optical spectra of AIE luminogens in the amorphous phase, exemplified by an emblematic AIE luminogen, hexaphenylsilole (HPS)[26,27] (see Fig. 1a). Our protocol successfully mapped the molecular packing of amorphous HPS aggregates at the atomic level to the AIE effects at the mesoscopic level. Consistent with the experimental observations,[26–28] the amorphous HPS aggregates convey almost unchanged absorption and redder emission with respect to that of crystals. Strikingly, the fluorescence quantum efficiency (FQE) of nanosized aggregates is size independent, leading to a linear relationship between the overall fluorescence intensity and the aggregate size. Moreover, our calculations provide a direct interpretation for the experimental crystallization enhanced emission (CEE) phenomenon of the propeller-shaped AIE luminogens.

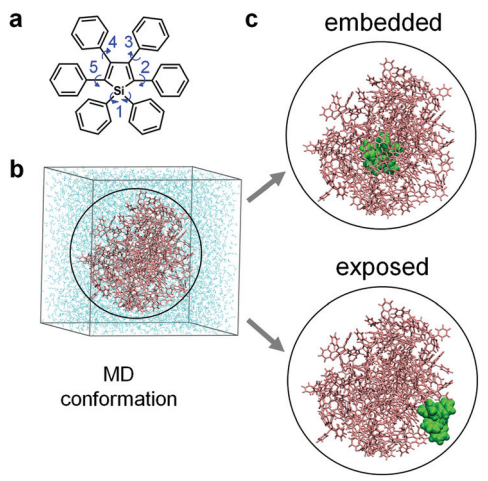

Fig. 1 Setup QM/MM models for amorphous HPS aggregates sampled by MD simulations. (a) Molecular structure of HPS with key dihedral angles between each phenyl group and the central silacycle highlighted by blue arrows. (b) HPS conformation extracted from the MD simulations. (c) The QM/MM model for each aggregate is set up by choosing one HPS molecule as the QM region and the others as the MM region. Embedded (top) and exposed (bottom) HPS molecules in the same aggregate have different packing densities and thus are treated separately.

Computational methods

MD simulations

To obtain the configurations of amorphous HPS aggregates with different sizes, we performed 25 MD simulations on HPS systems at five different concentrations in aqueous solution. The initial conformations were generated by randomly placing 10, 20, 30, 40 and 60 HPS molecules in the cubic simulation boxes with 4 nm edge length. To avoid interference with the boundaries, an additional layer of 2 nm width of pure water was added. The final simulation box size was $6 \times 6 \times 6$ nm^3. The total amount of water at concentrations from 10 to 60 was 6658, 6373, 6053, 5752, and 5137, respectively. The HPS systems prepared were more concentrated at the center of the simulation boxes because the aggregation process starting from a uniform distribution was prohibitively time-consuming.

The atom types and interaction parameters of HPS were mainly based on the general Amber force field (GAFF).[29] Since the parameter for Si was not available in the GAFF, we fitted the torsional angle parameters based on rigorous QM calculations. All other parameters for bond lengths and bond angles were inherited from our previous studies,[30,31] see more details in the ESI.† To validate our force field parameters, we performed five 20 ns MD simulations of the HPS supercell constructed based on the experimental HPS crystal structure.[26] The calculated average packing density of the HPS supercell well reproduced the corresponding packing density of the HPS crystal in the experiment, see details in the supplementary method and Fig. S3.† These results demonstrated the applicability of our force field to the current study of amorphous HPS aggregates.

For each system in aqueous solution, energy minimization was performed using the steepest descent algorithm, followed by 5 ns MD simulations under the NPT (P = 1 bar and T = 300 K) ensemble coupled by the velocity rescaling thermostat[32] and Berendsen barostat[33,34] with the time constants of both couplings 1.0 ps. The subsequently produced MD simulations for each system consist of five independent 20 ns NPT simulations with different initial velocities coupled by the velocity rescaling thermostat[32] and Parrinello–Rahman barostat[35]. For the electrostatic interactions, the reciprocal space summation was evaluated by the particle mesh Ewald (PME) method[36,37] and the direct space summation was computed at a cutoff distance of 1.2 nm. The cutoff distance for vdW interactions was 1.1 nm. All bond lengths were constrained *via* the LINCS algorithm.[38] Periodic boundary conditions were applied in all three dimensions to minimize the edge effects in a finite system. Different from the simulation of the HPS supercell, the time step for the HPS aggregation process was 2 fs. The configurations were stored at a time interval of 20 ps for data analysis.

QM/MM calculations

Based on the sufficient amorphous HPS conformations obtained from MD simulations, we randomly extracted HPS

aggregates and setup QM/MM models for them to calculate the optical properties. At each size, five conformations were extracted from the final 1 ns of each of the five MD trajectories (see Fig. 1b). Then, we obtained each HPS aggregate by removing all solvents from each extracted MD conformation. Different from the ordered packing in crystals, the molecular packing of amorphous HPS aggregates is irregular, resulting in distinct local environments for the embedded and exposed HPS molecules in each aggregate. Hence, we setup both embedded and exposed QM/MM models for each HPS aggregate. In the embedded QM/MM model, we randomly chose one completely enclosed HPS molecule from the aggregate and treated it as the QM region while all others as the MM region (see top of Fig. 1c). Alternatively, in the exposed QM/MM model, one HPS molecule exposed at the surface of the HPS aggregate was handled as the QM region (see bottom of Fig. 1c). The central QM region provides key information of the electronic excited-state while the MM region could include important corrections from the environment. Here the excitonic effect, the intermolecular charge transfer and the polarizable effect were neglected, because of the large intermolecular distance in amorphous HPS aggregates.[31] At each size, five embedded QM/MM models were setup for all five extracted aggregates, while one exposed QM/MM model was setup for one of the five extracted aggregates. The QM/MM calculations were performed by using the ChemShell package[39] interfacing TURBOMOLE[40] and DLPLOY[41] programs. Herein, we adopted (TD)B3LYP/SV(P)[42] for QM, the GAFF[29] for MM, with the electrostatic embedding scheme[43,44] for the QM/MM treatments. In addition, the QM molecule was active and the MM molecules were frozen during the geometry optimization. The numerical differentiation method was used to calculate the vibrational frequency and the polarization effect of the environment was included.

Radiative and non-radiative decay rate constants' calculations

The radiative decay rate constant (k_r) was calculated by integrating over the whole emission spectra:

$$k_r(T) = \int \sigma_{\mathrm{em}}(\omega, T)\mathrm{d}\omega \tag{1}$$

$$\sigma_{\mathrm{em}}(\omega, T) = \frac{4\omega^3}{3\hbar c^3}\sum_{u,\nu} P_{\mathrm{i}\nu}(T)\left|\langle \Theta_{\mathrm{f}u}|\vec{\mu}_{\mathrm{fi}}|\Theta_{\mathrm{i}\nu}\rangle\right|^2 \delta\left(\omega_{\mathrm{i}\nu,\mathrm{f}u} - \omega\right) \tag{2}$$

Here $P_{\mathrm{i}\nu}$ is the Boltzmann distribution function of the initial state at a specific temperature. Θ is the nuclear vibrational wave function. $\vec{\mu}_{fi} = \langle \Phi_f|\vec{\mu}|\Phi_i\rangle$ is the electric transition dipole moment between two electronic states.

Based on the Fermi Golden rule, the non-radiative internal conversion (IC) decay rate constant can be formulated as:[45]

$$k_{IC} = \frac{2\pi}{\hbar}\sum_{u,\nu} P_{i\nu}\left|\hat{H}'_{fu,i\nu}\right|^2 \delta\left(E_{i\nu} - E_{fu}\right) \tag{3}$$

where $E_{\mathrm{i}\nu}(E_{\mathrm{f}u})$ reflects the electronic and vibrational energy of the initial (final) state, $\hat{H}'$ represents the non-Born–Oppenheimer coupling.

Based on the Franck–Condon principle, applying Fourier transform of the δ-function, eqn (3) can be written as:[46,47]

$$k_{IC} = \sum_{kl}\frac{1}{\hbar^2}R_{kl}\int_{-\infty}^{\infty} dt\left[e^{i\omega_{ij}t}Z_i^{-1}\rho_{IC}(t,T)\right] \tag{4}$$

where $R_{kl} = \langle\Phi_{\mathrm{f}}|\hat{P}_{\mathrm{f}k}|\Phi_{\mathrm{i}}\rangle\langle\Phi_{\mathrm{i}}|\hat{P}_{\mathrm{f}l}|\Phi_{\mathrm{f}}\rangle$ is the non-adiabatic electronic coupling. $\rho_{\mathrm{IC}}(t, T)$ is the thermal vibration correlation function (TVCF),[22,48,49]

$$\rho_{\mathrm{IC},kl}(t,T) = \mathrm{Tr}(\hat{P}_{\mathrm{f}k}\mathrm{e}^{-i\tau_{\mathrm{f}}\hat{H}_{\mathrm{f}}}\hat{P}_{\mathrm{f}l}\mathrm{e}^{-i\tau_{\mathrm{i}}\hat{H}_{\mathrm{i}}}). \tag{5}$$

Based on the electronic structure information obtained from QM/MM optimization, the radiative and non-radiative rate constants were calculated by solving eqn (1) and (3) through the TVCF in the home-built MOMAP program.[50] The difference between the potential energy surfaces of the ground and excited states is considered by $Q_{\mathrm{i}} = \mathbf{S}\mathbf{Q}_{\mathrm{f}} + \mathbf{D}$, where $\mathbf{S}$ is the Duschinsky rotation matrix and $\mathbf{D}$ is the displacement vector. The non-adiabatic electronic couplings were calculated by using the exact analytical derivative couplings between the time-dependent Kohn–Sham determinants in a finite atom-centered basis set in TURBOMOLE program.[51]

Results and discussion

Molecular packing of amorphous HPS aggregates

The amorphous HPS aggregates are obtained by long time atomistic MD simulations in aqueous solution. The aggregation process of HPS molecules is fast and mainly driven by hydrophobic interactions (see Fig. S4–S7† for details). The morphology of HPS aggregates is generally near spherical, except for small aggregates (see Fig. 2a). We used the asphericity parameter, Ap (see definition in the ESI†) to measure the aggregate morphology (spherical when Ap = 0 and rod when Ap = 1). For simplicity, the aggregates with sizes 10, 20, 30, 40 and 60, are referred to as Agg-10, Agg-20, Agg-30, Agg-40 and Agg-60, respectively hereafter. As shown in Fig. 2a, it is clear that, from Agg-60 to Agg-20, all Ap distributions are dominated by a single peak, except for Agg-10 where HPS molecules are too few to form the complete packing. In addition, Ap generally decreases as the aggregate size grows.

The packing density of HPS aggregates for all systems is size independent and smaller than that of crystals (see Fig. 2b and S3†). The average RDFs (*vs.* the intermolecular Si–Si distance) of HPS aggregates are featured by a single major peak within a small range of 8.8 Å–9.4 Å for all systems (see Fig. 2c), pointing to the similar molecular packing of HPS aggregates of different sizes and a linear relationship between the aggregate size and volume (see Fig. S7†). Importantly, the width of all RDF curves of HPS aggregates is larger than that of crystals, indicating a looser molecular packing in amorphous aggregates than in crystals (see Fig. 2b, c and S8†). The intermolecular distances, depending on the molecular packing of the aggregates, could influence the relative motions of HPS molecules in aggregates and ultimately determine their optical

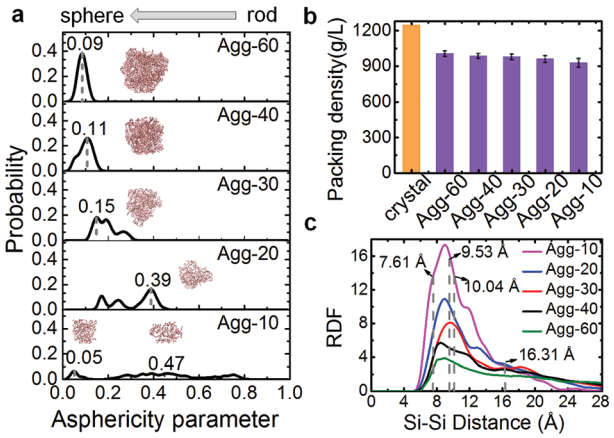

Fig. 2 Morphology and molecular packing of the amorphous HPS aggregates. (a) The asphericity parameter (Ap) distribution of the amorphous HPS aggregates at various sizes. For each distribution, the Ap value and the location of the Ap peak are labelled, respectively, with one representative snapshot of the HPS aggregate nearby. (b) The average packing density of amorphous HPS aggregates. The value for crystals is also shown for comparison. (c) The average radical distribution functions (RDFs) as a function of the intermolecular Si–Si distance. All HPS aggregates are extracted from the last 2 ns of five MD trajectories at each concentration. The lattice constants of the HPS crystal (CCDC 195948):[26] a = 9.53 Å, b = 10.04 Å and c = 16.31 Å, and the intermolecular distance of two HPS molecules in the unit cell (7.61 Å) are shown by dashed lines in c for comparison.

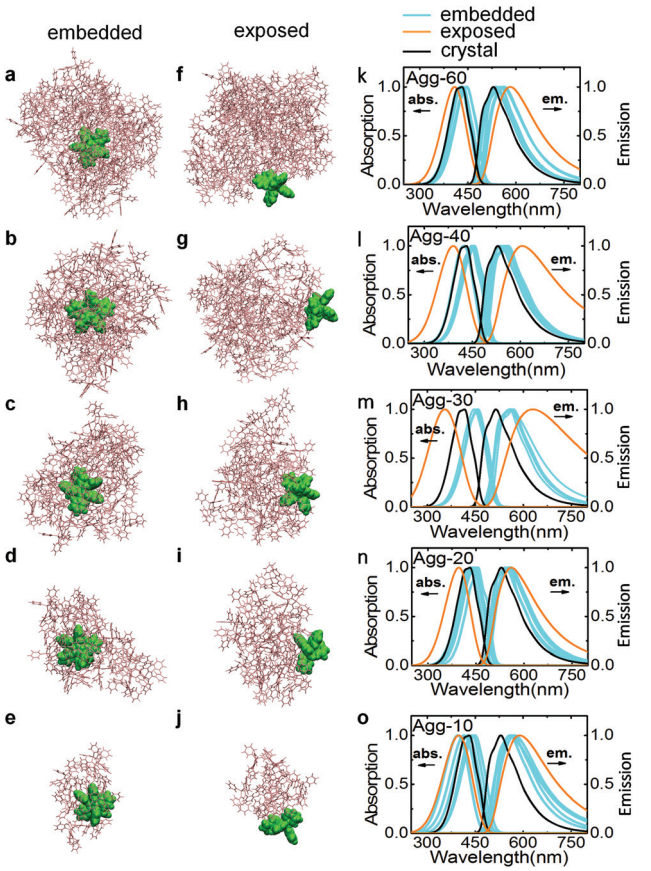

Fig. 3 The representative QM/MM models including the (a–e) embedded and (f–j) exposed cases, as well as (k–o) the calculated vibrationally resolved normalized absorption (left) and emission (right) spectra for five embedded (cyan line) and one exposed HPS molecule (orange line) in aggregates with different sizes. The corresponding spectra of the HPS crystal are shown (black line) for comparison.

properties. Therefore these structural analyses suggest that the optical properties of amorphous HPS aggregates could be significantly different from those of crystals.

Vibrationally resolved optical spectra of amorphous HPS aggregates

Although the packing density of HPS aggregates is size independent, the environments between the embedded and exposed HPS molecules in each aggregate are very different. Therefore, we randomly extracted five amorphous HPS aggregates from MD simulations at each size, and then calculated the vibrational resolved spectra of embedded and exposed HPS molecules. We prepared five embedded and one exposed QM/MM models at each size (see Fig. 3a–e and Fig. 3f–j), with one embedded/exposed HPS molecule as the QM region and the others as the MM region (details in Computational methods). For Agg-10, the HPS aggregate is too small to completely enclose any HPS molecule, leading to near-identical optical properties between the partially embedded and exposed HPS molecules in Agg-10. Therefore, the embedded cases for Agg-10 are not discussed hereafter.

The calculated spectra for the amorphous aggregates barely vary with the aggregate size. The absorption is similar to that of crystals while the emission is clearly redshifted from the crystalline one. At each size, both the absorption and emission spectra for the five embedded HPS molecules are similar, but considerably distinguishable from those of the exposed one. Compared to exposed HPS, the absorption spectra of the embedded HPS exhibit a redshift, with the maximum peak wavelength $l_{abs,embedded} > l_{abs,exposed}$. This is supported by the lower energy gaps of the embedded HPS molecules at S_0 than that of the exposed one, see Table S3,† because the embedded HPS molecules exhibit a more planar and better conjugation than the exposed one, as evidenced by the smaller torsional angles of the phenyl groups at 2,5-positions relative to the central silacycle (see Tables 1, S1 and S2†), which mainly takes part in the electronic transition (see Fig. 4). Interestingly, the absorption of HPS in crystals always occurs between those of the embedded and exposed HPS molecules in amorphous aggregates ($l_{abs,embedded} > l_{abs,crystal} > l_{abs,exposed}$). Therefore, the overall absorption of the aggregate (embedded plus exposed HPS molecules) remains similar to that of crystals, consistent with the experimental observations.[26]

In clear contrast, the emission spectra obviously redshift from the crystal to embedded, and then to exposed HPS molecules in each aggregate ($l_{em,exposed} > l_{em,embedded} > l_{em,crystal}$, see Fig. 3k–o, Table S4†), which well reproduces the experimental observations.[26–28] This can be explained by the lower packing density induced larger reorganization energies in amorphous

Table 1 The optimized dihedral angles (in degree) of one representative embedded and exposed HPS molecule in the HPS aggregate, at each size. S_0/S_1 and Δ represent the geometric parameters extracted from the ground/excited states, and the difference between them, respectively

	Agg-60			Agg-40			Agg-30			Agg-20			Agg-10		
	S_0	S_1	Δ	S_0	S_1	Δ	S_0	S_1	Δ	S_0	S_1	Δ	S_0	S_1	Δ
Embedded															
2-	32.67	27.92	4.75	−31.29	−24.33	6.96	23.56	18.48	5.08	−20.78	−17.64	3.14	−43.36	−32.63	10.73
5-	20.26	17.13	3.13	−14.38	−14.07	0.31	24.72	23.14	1.58	−11.17	−9.11	2.06	−24.01	−19.02	4.99
3-	57.67	52.66	5.01	−55.56	−52.41	3.15	49.83	45.49	4.34	−63.97	−54.02	9.95	−56.39	−52.78	3.61
4-	56.96	50.81	6.15	−61.92	−58.02	3.90	56.16	54.33	1.83	−72.08	−70.85	1.23	−62.63	−53.80	8.83
Exposed															
2-	−36.13	−26.21	9.92	−45.09	−28.12	16.97	39.45	22.98	16.47	29.80	21.47	8.33	−28.10	−25.42	2.68
5-	−25.37	−18.86	6.51	−35.81	−24.88	10.93	24.32	20.10	4.22	27.45	20.74	6.71	−18.06	−18.83	0.77
3-	−49.59	−46.00	3.59	−51.25	−47.48	3.77	58.31	45.99	12.32	58.64	50.27	8.37	−62.49	−61.05	1.44
4-	−64.77	−57.42	7.35	−57.48	−54.19	3.29	66.02	65.24	0.78	60.77	54.37	6.40	−68.17	−49.98	18.19

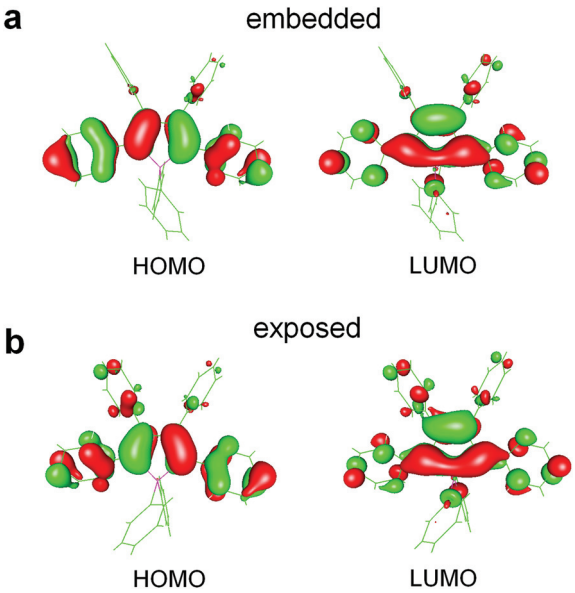

Fig. 4 The electron density contours of HOMO and LUMO for the (a) embedded and (b) exposed HPS molecules of one representative amorphous aggregate Agg-60.

HPS aggregates as compared to that in crystals (see Fig. 6a and 7a), which is similar to the case of HPS in the gas phase.[30] In addition, the mirror-image symmetry between each pair of absorption and emission spectra is broken, due to the torsional and Duschinsky rotational effects of the potential energy surfaces between S_0 and S_1,[52] see Fig. 3k–o.

Size independent fluorescence quantum efficiency of amorphous HPS aggregates

Strikingly, the fluorescence quantum efficiency (FQE), calculated by $\eta_F \approx k_r/(k_r + k_{IC})$,[30,31] of the embedded HPS molecules (>92.7%) is size independent and is 1–2 orders of magnitude larger than those of the exposed ones (<7%), see Table 2 and Fig. 5. Here, k_r and k_{IC} are the radiative decay rate constant and the internal conversion (IC) decay rate constant, respectively, see details in Computational methods. The large FQE of

Table 2 The calculated k_r, k_{IC} and FQE (η_F) for the five embedded and one exposed HPS molecule in aggregates, at each size. The parameters for the HPS crystal are included for comparison. The error bars are listed in parenthesis

System	k_r (10^7 s^{-1})	k_{IC} (10^7 s^{-1})	η_F (%)
Crystal (cal.)[a]	7.43	0.16	97.9
Embedded			
Agg-60	6.16 (1.09)	0.51 (0.26)	92.7 (3.4)
Agg-40	5.72 (1.03)	0.20 (0.30)	95.3 (4.6)
Agg-30	7.08 (3.47)	0.30 (0.43)	96.8 (3.3)
Agg-20	5.97 (1.03)	0.26 (0.20)	95.7 (2.6)
Agg-10	3.77 (1.89)	37.2 (42.03)	34.9 (32.3)
Exposed			
Agg-60	4.45	64.9	6.42
Agg-40	2.85	320	0.80
Agg-30	4.55	4830	0.09
Agg-20	4.96	72.1	6.43
Agg-10	4.54	329	1.36

[a] Ref. 31.

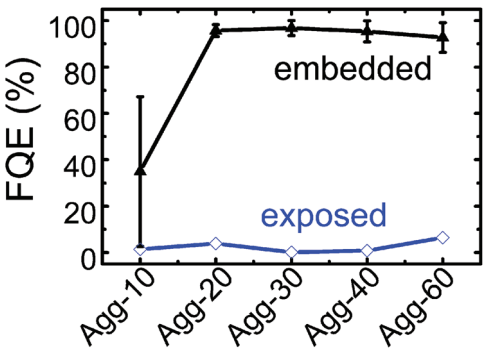

Fig. 5 The average fluorescence quantum efficiency (FQE) of five embedded and one exposed HPS molecule in amorphous aggregates with different sizes.

embedded HPS molecules is mainly caused by a much smaller k_{IC} and almost unchanged k_r compared to those of the exposed ones (see Table 2). These significantly different FQE between embedded and exposed HPS could be attributed to their

different surrounding environments, *i.e.* the extent of molecular packing influences the intramolecular vibrational motions and dictates the nonradiative decay rates. For all embedded HPS molecules, the molecular packing is almost equally tight and lays restrictions on their intramolecular vibrational motions to a similarly strong extent, and therefore leads to similar high FQE values. For the exposed HPS, the restrictions of the surrounding environment on their intramolecular vibrational motions are much weaker, yielding negligible FQE values.

Consistent with previous observations,[30] the radiative decay process is insensitive to the surrounding environments, and its k_r is independent of the aggregation size for all HPS aggregates, including either embedded or exposed HPS molecules, see Table 2. This is mainly because the electronic transition property is immune to the environment, which leads to the slightly changed adiabatic excitation energy (ΔE) and transition dipole moment (μ), determining the k_r (see Table S5†).

In clear contrast to the radiative decay process, the nonradiative decay process is very sensitive to the environment. The average k_{IC} values of embedded HPS molecules are similar for all systems and are all 2–4 orders of magnitude smaller than those of the exposed ones (see Table 2). Different from the radiative decay induced by the transition dipole, the nonradiative decay is generated by the molecular thermal vibrational motions that can be quantified by the reorganization energy λ. It is the considerably smaller λ of the embedded HPS molecules than the exposed ones that leads to the much slower nonradiative decay rate of the former than the latter. As shown in Fig. 6a, the average overall (λ_{total}), ground-state (λ_{gs}) and excited-state (λ_{es}) reorganization energies of embedded HPS molecules are size independent and all around the values for crystals. For exposed HPS, the corresponding λ values are all larger than the crystal values and close to the value of the isolated HPS molecule (gas phase), see Fig. 7a.

To further understand the exact source of the reorganization energy λ, we projected it onto different geometrical internal coordinates of the HPS molecules. We found that both the λ_{bond} and λ_{angle} of HPS molecules fall in a small range of values in all phases of all systems, while the $\lambda_{dihedral}$ of embedded HPS molecules are slightly larger than that for crystals and much smaller than those of the exposed ones (close to that of the gas phase), see Fig. 6b–d and 7b–d, respectively. For both the embedded and exposed HPS molecules, we mainly present the torsional angles of the phenyl groups at 2,3,4,5-positions relative to the central silacycle. These torsional angles are in charge of the low-frequency normal modes with a large reorganization energy and their corresponding modes of motions are greatly susceptible to the surrounding molecular packing. Unlike exposed HPS, such modes of motions of these important torsional angles in embedded HPS molecules are largely suppressed, consistent with the corresponding geometrical modifications from S_1 to S_0, see Tables 1, S1 and S2.† The structural differences Δ between the minima of S_0 and S_1 of the exposed HPS are considerably larger than those of embedded ones. Because the geometrical modification of the exposed HPS molecules from S_0 to S_1 is very large, their corresponding excited-state energies are mostly converted to heat nonradiatively.

More excitingly, the size independent fluorescence quantum efficiency predicts a linear relationship between the fluorescence intensity and aggregate size of the nanosized

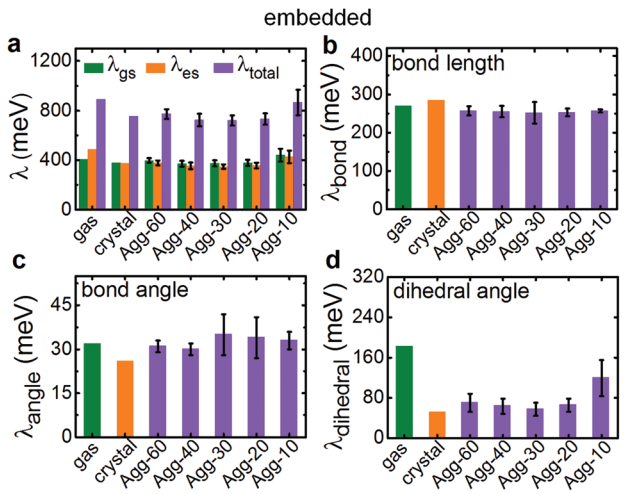

Fig. 6 Reorganization energy of embedded HPS molecules in amorphous aggregates, including averaged (a) overall (λ_{total}), ground-state (λ_{gs}) and excited-state (λ_{es}). The projection of λ_{es} onto the internal coordinates of the HPS molecule, *e.g.* (b) bond length, (c) bond angle and (d) dihedral angle, respectively. The corresponding values in the gas and crystal phases are illustrated for comparison.

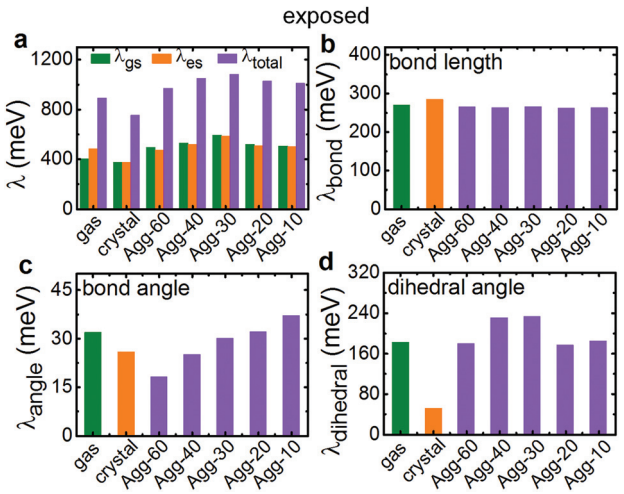

Fig. 7 Reorganization energy of the exposed HPS molecules in amorphous aggregates, including (a) overall (λ_{total}), ground-state (λ_{gs}) and excited-state (λ_{es}). The projection of λ_{es} onto the internal coordinates of the HPS molecule, *e.g.* (b) bond length, (c) bond angle and (d) dihedral angle, respectively. The corresponding values in the gas and crystal phases are illustrated for comparison.

amorphous HPS aggregates. The experimentally obtained amorphous HPS aggregates are usually nanosized and generally spherical (see Fig. 2a). Such large aggregates contain a much higher ratio of embedded HPS molecules and a negligible fraction of the exposed ones. As a result, the optical properties and the FQE of nanosized amorphous aggregates are mainly determined by the embedded HPS molecules. Since the ratio of embedded HPS molecules increases as the aggregate size increases and since the FQE of amorphous HPS aggregates is size independent, one naturally deduces that the fluorescence intensity has a linear relationship with the aggregate size.

Interpretation of the crystallization enhanced emission phenomenon in experiments

In experiments, amorphizing the HPS crystal by grinding leads to a redder and weaker emission, known as crystallization-enhanced emission (CEE).[18,27,28,53,54] Despite its crucial role in mechanochromic luminogens' design and applications, the mechanism underlying CEE is still unclear. Notably, our calculations could well explain the CEE phenomenon through the redshift of the emission and the reduced fluorescence intensity of HPS from the crystalline to amorphous phases. Firstly, grinding the crystal increases the fraction of amorphous aggregates and reduces the overall packing density (see Fig. 2b). Accordingly, the reduced packing density in the amorphous aggregates results in a redshift of the emission (see Fig. 3k–o). Secondly, grinding also increases the exposed surface area of HPS aggregates, *i.e.* increases the ratio of exposed HPS molecules. Since the FQE is size independent and the FQE of exposed HPS molecules is considerably smaller than those of embedded and crystalline ones, such an increased ratio of the exposed HPS naturally leads to a sharp decrease of the overall FQE and a heavily weakened fluorescence intensity of the aggregates (see Table 2 and Fig. 5). Collectively, the decreased molecular packing density and increased ratio of exposed HPS molecules by grinding well explain the CEE effect in propeller-shaped AIE luminogens.

Conclusions

We explored the mechanism of aggregation-induced emission of the amorphous HPS aggregates by using a theoretical protocol that combines molecular dynamics (MD) simulation, and the correlation function rate formalism coupled hybrid quantum mechanics/molecular mechanics (QM/MM) method. MD simulations are performed to obtain various conformations of amorphous HPS aggregates. The correlation function rate formalism coupled with QM/MM calculations is used to obtain the optimized electronic structures, reorganization energy, vibrationally resolved spectra, radiative and non-radiative decay rate constants and fluorescence quantum efficiency (FQE).

We demonstrated that the packing density of amorphous HPS aggregates is size independent and is lower than that of crystals, leading to their weaker and redder emission than their crystals. However, the radiative decay process is immune to the molecular packing environment due to the almost unchanged electronic transition properties. However, the non-radiative decay process is very susceptible to the molecular packing environment. The resultant non-radiative decay rate constants of the embedded HPS molecules are 2–4 orders of magnitude smaller than those of the exposed ones, because the intramolecular low-frequency vibrational motions are restricted by the tight molecular packing. In accordance with this, the FQE of embedded HPS molecules is considerably larger than that of the exposed ones. Owing to the high ratio of embedded HPS molecules in nanosized amorphous aggregates and their size independent FQE, the fluorescence intensity of amorphous aggregates exhibits a linear relationship with the aggregate size. Such a linear relationship indicates that the fluorescence intensity of propeller-shaped amorphous AIE luminogens can be an effective gauge to monitor their aggregate size in experiments. In addition, our results could well explain the crystallization-enhanced emission phenomenon in experiments. Our theoretical protocol successfully elucidates the relationship between the molecular packing, optical spectra and FQE of HPS in all different phases. This protocol is general and applicable to the study of the optical properties of other AIE luminogens, such as tetraphenylethene (TPE) and its derivatives.[55] We believe that the systematic knowledge on the structure–property relationship behind the AIE phenomenon could pave the way for the rational design of advanced AIE materials.

Acknowledgements

This work is financially supported by the National Basic Research Program of China (973 program, Grant No. 2013CB834703), and the National Natural Science Foundation of China (21273188, 21290191, 21473214), the Innovation and Technology Commission (ITC-CNERC14SC01).

Notes and references

1 R. T. K. Kwok, C. W. T. Leung, J. W. Y. Lam and B. Z. Tang, *Chem. Soc. Rev.*, 2015, **44**, 4228–4238.
2 J. Mei, N. L. C. Leung, R. T. K. Kwok, J. W. Y. Lam and B. Z. Tang, *Chem. Rev.*, 2015, **115**, 11718–11940.
3 M. Vendrell, D. Zhai, J. C. Er and Y.-T. Chang, *Chem. Rev.*, 2012, **112**, 4391–4420.
4 D. Ding, K. Li, B. Liu and B. Z. Tang, *Acc. Chem. Res.*, 2013, **46**, 2441–2453.
5 L. Yan, Y. Zhang, B. Xu and W. Tian, *Nanoscale*, 2016, **8**, 2471–2487.
6 J. B. Briks, *Photophysics of Aromatic Molecules*, Wiley, London, 1970.
7 R. Deans, J. Kim, M. R. Machacek and T. M. Swager, *J. Am. Chem. Soc.*, 2000, **122**, 8565–8566.

8 M. Levitus, K. Schmieder, H. Ricks, K. D. Shimizu, U. H. F. Bunz and M. A. Garcia-Garibay, *J. Am. Chem. Soc.*, 2001, **123**, 4259–4265.
9 C. Belton, D. F. O'Brien, W. J. Blau, A. J. Cadby, P. A. Lane, D. D. C. Bradley, H. J. Byrne, R. Stockmann and H.-H. Hörhold, *Appl. Phys. Lett.*, 2001, **78**, 1059–1061.
10 J. Luo, Z. Xie, J. W. Y. Lam, L. Cheng, H. Chen, C. Qiu, H. S. Kwok, X. Zhan, Y. Liu, D. Zhu and B. Z. Tang, *Chem. Commun.*, 2001, 1740–1741.
11 M. C. Traub, J. Vogelsang, K. N. Plunkett, C. Nuckolls, P. F. Barbara and D. A. Vanden Bout, *ACS Nano*, 2012, **6**, 523–529.
12 A. J. Gesquiere, T. Uwada, T. Asahi, H. Masuhara and P. F. Barbara, *Nano Lett.*, 2005, **5**, 1321–1325.
13 B.-K. An, S.-K. Kwon, S.-D. Jung and S. Y. Park, *J. Am. Chem. Soc.*, 2002, **124**, 14410–14415.
14 X. Yan, T. R. Cook, P. Wang, F. Huang and P. J. Stang, *Nat. Chem.*, 2015, **7**, 342–348.
15 A. Satrijo and T. M. Swager, *J. Am. Chem. Soc.*, 2007, **129**, 16020–16028.
16 T. He, X. Tao, J. Yang, D. Guo, H. Xia, J. Jia and M. Jiang, *Chem. Commun.*, 2011, **47**, 2907–2909.
17 T. Tachikawa, H.-R. Chung, A. Masuhara, H. Kasai, H. Oikawa, H. Nakanishi, M. Fujitsuka and T. Majima, *J. Am. Chem. Soc.*, 2006, **128**, 15944–15945.
18 Y. Q. Dong, J. W. Y. Lam and B. Z. Tang, *J. Phys. Chem. Lett.*, 2015, **6**, 3429–3436.
19 T. Han, Y. Hong, N. Xie, S. Chen, N. Zhao, E. Zhao, J. W. Y. Lam, H. H. Y. Sung, Y. Dong, B. Tong and B. Z. Tang, *J. Mater. Chem. C*, 2013, **1**, 7314–7320.
20 Y. Hong, J. W. Y. Lam and B. Z. Tang, *Chem. Commun.*, 2009, 4332–4353.
21 J. Mei, Y. Hong, J. W. Y. Lam, A. Qin, Y. Tang and B. Z. Tang, *Adv. Mater.*, 2014, **26**, 5429–5479.
22 Z. Shuai and Q. Peng, *Phys. Rep.*, 2014, **537**, 123–156.
23 G. Sun, Y. Zhao and W. Liang, *J. Chem. Theory Comput.*, 2015, **11**, 2257–2267.
24 Q. Peng, Y. Yi, Z. Shuai and J. Shao, *J. Am. Chem. Soc.*, 2007, **129**, 9333–9339.
25 Q. Wu, Q. Peng, Y. Niu, X. Gao and Z. Shuai, *J. Phys. Chem. A*, 2012, **116**, 3881–3888.
26 J. Chen, C. C. W. Law, J. W. Y. Lam, Y. Dong, S. M. F. Lo, I. D. Williams, D. Zhu and B. Z. Tang, *Chem. Mater.*, 2003, **15**, 1535–1546.
27 Y. Dong, J. Y. Lam, Z. Li, A. Qin, H. Tong, Y. Dong, X. Feng and B. Tang, *J. Inorg. Organomet. Polym.*, 2005, **15**, 287–291.
28 Y. Dong, J. Y. Lam, A. Qin, Z. Li, J. Sun, Y. Dong and B. Tang, *J. Inorg. Organomet. Polym.*, 2007, **17**, 673–678.
29 J. Wang, R. M. Wolf, J. W. Caldwell, P. A. Kollman and D. A. Case, *J. Comput. Chem.*, 2004, **25**, 1157–1174.
30 T. Zhang, Y. Jiang, Y. Niu, D. Wang, Q. Peng and Z. Shuai, *J. Phys. Chem. A*, 2014, **118**, 9094–9104.
31 (*a*) Y. Xie, T. Zhang, Z. Li, Q. Peng, Y. Yi and Z. Shuai, *Chem. – Asian J.*, 2015, **10**, 2154–2161; (*b*) X. Tao and Y. ShiWei, *Sci. China: Chem.*, 2014, **57**(10), 1375–1382.
32 G. Bussi, D. Donadio and M. Parrinello, *J. Chem. Phys.*, 2007, **126**, 014101.
33 H. J. C. Berendsen, J. P. M. Postma, W. F. van Gunsteren, A. DiNola and J. R. Haak, *J. Chem. Phys.*, 1984, **81**, 3684–3690.
34 H. Berendsen, J. Postma, W. van Gunsteren and J. Hermans, in *Intermolecular Forces*, Reidel, Dordrecht, 1981, pp. 331–342.
35 M. Parrinello and A. Rahman, *J. Appl. Phys.*, 1981, **52**, 7182–7190.
36 T. Darden, D. York and L. Pedersen, *J. Chem. Phys.*, 1993, **98**, 10089–10092.
37 U. Essmann, L. Perera, M. L. Berkowitz, T. Darden, H. Lee and L. G. Pedersen, *J. Chem. Phys.*, 1995, **103**, 8577–8593.
38 B. Hess, H. Bekker, H. J. C. Berendsen and J. G. E. M. Fraaije, *J. Comput. Chem.*, 1997, **18**, 1463–1472.
39 P. Sherwood, A. H. de Vries, M. F. Guest, G. Schreckenbach, C. R. A. Catlow, S. A. French, A. A. Sokol, S. T. Bromley, W. Thiel, A. J. Turner, S. Billeter, F. Terstegen, S. Thiel, J. Kendrick, S. C. Rogers, J. Casci, M. Watson, F. King, E. Karlsen, M. Sjøvoll, A. Fahmi, A. Schäfer and C. Lennartz, *J. Mol. Struct. (THEOCHEM)*, 2003, **632**, 1–28.
40 R. Ahlrichs, M. Bär, M. Häser, H. Horn and C. Kölmel, *Chem. Phys. Lett.*, 1989, **162**, 165–169.
41 W. Smith and T. R. Forester, *J. Mol. Graphics*, 1996, **14**, 136–141.
42 F. Weigend, M. Häser, H. Patzelt and R. Ahlrichs, *Chem. Phys. Lett.*, 1998, **294**, 143–152.
43 J. Aaqvist and A. Warshel, *Chem. Rev.*, 1993, **93**, 2523–2544.
44 H. Lin and D. G. Truhlar, *Theor. Chem. Acc.*, 2007, **117**, 185–199.
45 S. H. Lin, C. H. Chang, K. K. Liang, R. Chang, Y. J. Shiu, J. M. Zhang, T. S. Yang, M. Hayashi and F. C. Hsu, *Adv. Chem. Phys.*, 2002, **121**, 1–88.
46 Y. Niu, Q. Peng and Z. Shuai, *Sci. China, Ser. B: Chem.*, 2008, **51**, 1153–1158.
47 Q. Peng, Y. Yi, Z. Shuai and J. Shao, *J. Chem. Phys.*, 2007, **126**, 114302.
48 Q. Peng, Y. Niu, Q. Shi, X. Gao and Z. Shuai, *J. Chem. Theory Comput.*, 2013, **9**, 1132–1143.
49 Y. Niu, Q. Peng, C. Deng, X. Gao and Z. Shuai, *J. Phys. Chem. A*, 2010, **114**, 7817–7831.
50 Z. Shuai, Q. Peng, Y. Niu and H. Geng, *Revision 0.2.004*, Beijing, China, 2014, available online: http://www.shuaigroup.net/, DOI: 10.1002/jcc.23365.
51 R. Send and F. Furche, *J. Chem. Phys.*, 2010, **132**, 044107.
52 Y. Jiang, Q. Peng, X. Gao, Z. Shuai, Y. Niu and S. H. Lin, *J. Mater. Chem.*, 2012, **22**, 4491–4501.
53 Y. Dong, J. W. Y. Lam, A. Qin, Z. Li, J. Sun, H. H. Y. Sung, I. D. Williams and B. Z. Tang, *Chem. Commun.*, 2007, 40–42.
54 Y. Dong, J. W. Y. Lam, A. Qin, J. Sun, J. Liu, Z. Li, J. Sun, H. H. Y. Sung, I. D. Williams, H. S. Kwok and B. Z. Tang, *Chem. Commun.*, 2007, 3255–3257.
55 Z. Zhao, J. W. Y. Lam and B. Z. Tang, *J. Mater. Chem.*, 2012, **22**, 23726–23740.

